Near-field analysis of terahertz pulse generation from photo-excited charge density gradients

Raimund Mueckstein, Michele Natrella, Osama Hatem, Joshua R. Freeman, Chris S. Graham, Cyril C. Renaud, Alwyn J. Seeds, Edmund H. Linfield, A. Giles Davies, Paul J. Cannard, Mike J. Robertson, Dave G. Moodie, and Oleg Mitrofanov

***Abstract*— Excitation of photo-current transients at semiconductor surfaces by sub-picosecond optical pulses gives rise to emission of electromagnetic pulses of terahertz (THz) frequency radiation. To correlate the THz emission with the photo-excited charge density distribution and the photo-current direction, we mapped near-field and far-field distributions of the generated THz waves from GaAs and Fe-doped InGaAs surfaces. The experimental results show that the charge dynamics in the plane of the surface can radiate substantially stronger THz pulses than the charge dynamics in the direction normal to the surface, which is generally regarded as the dominant origin of the emission.**

***Index Terms*—aperture, Dember effect, far-field radiation pattern, near-field radiation, near-field microscopy, emission pattern, pulse generation, terahertz.**

I. Introduction

The excitation of semiconductor surfaces by sub-picosecond optical pulses can lead to emission of picosecond pulses of terahertz (THz) frequency radiation [1-5]. Instrumental for THz time-domain spectroscopy, this effect has been explained by two mechanisms. In the first, the intrinsic (built-in) electric field owing to Fermi-level pinning at the surface causes a surge of photo-current in the direction normal to the surface [2]. This process was found to be dominant in semiconductors with a relatively wide bandgap (e.g. GaAs) [6,7]. On the other hand, for narrow bandgap semiconductors (such as InAs), with a small built-in electric field, the emission is attributed to a second process, the ambipolar diffusion of photo-carriers (the photo-Dember effect), which results in a net photo-current, also normal to the surface [8-12]. Different mobilities for holes and electrons and asymmetric carrier density distribution, caused by the semiconductor-air interface, are essential for the latter effect.

For efficient out-coupling of the THz emission due to the normal photo-current, the semiconductor surface is typically oriented at 45°-75° with respect to the optical axis [1-3]. More recently, photo-currents within the plane of the semiconductor surface were harnessed as a process for THz pulse generation [13-18]. Using normal incidence optical excitation, significant emission was observed in systems with an asymmetric photo-excited charge density distribution across the surface formed at the edge of a metallic contact [13,14]. There is some debate over the mechanism of this THz emission, named the lateral photo-Dember effect. In particular over the roles of the metallic contact and the photo-excited charge density gradient. The work in Refs. 13 and 15 suggest that the metal layer is not required if a high gradient is present, whereas Refs. 16-18 suggest that the metal layer is crucial for emission. This has raised questions over the distribution of photo-current responsible for the lateral photo-Dember effect.

The observation of THz radiation due to this in-plane charge carrier dynamic raises a more fundamental question, central to understanding the process of THz pulse generation and exploiting this effect: how significant is carrier movement in the surface plane in comparison to the movement normal to the surface? These questions remain unanswered despite a large body of investigations.

In this article, we describe experiments designed to correlate the emission of THz pulses, in both the near-field and far-field, with the photo-current distribution. Mapping the emitted THz wave in the near-field zone of a photo-excited semiconductor surface allows us to investigate the radiation from specific locations, in particular near the edges of an illuminated region, where a gradient of photo-carrier density is created along the surface. The near-field maps also allow us to identify the photo-current direction. The method is applied to investigate the process of excitation of epitaxial layers of Fe-doped $In_{0.53}Ga_{0.47}As$ (Fe:InGaAs) [19].

Remarkably, the experimental results show that the generated THz pulses originate primarily from the edge regions of the photo-excited area and therefore the lateral

This work was supported in part by the EPSRC under 'COTS' Programme Grant EP/J017671/1; the Royal Society under Grant U080745; the Royal Society and Wolfson Foundation, and the ERC under Grant 'TOSCA'.

R. Mueckstein was with Electronic and Electrical Engineering Department, University College London, London, WC1E 7JE, UK. He is now with Sirona Dental Systems GmbH, Bensheim, Germany.

M. Natrella, C. S. Graham, C. C. Renaud, A. J. Seeds are with Electronic and Electrical Engineering Department, University College London, London, WC1E 7JE, UK.

O. Hatem, J. R. Freeman, E. H. Linfield, A. G. Davies are with the School of Electronic and Electrical Engineering, University of Leeds, Leeds LS2 9JT, UK. O. Hatem is on leave from the Department of Engineering Physics and Mathematics, Tanta University, Egypt.

P. J. Cannard, M. J. Robertson, and D. G. Moodie, are with CIP Technologies (now Huawei), Adastral Park, Martlesham Heath, Ipswich, Suffolk, IP5 3RE, UK.

O. Mitrofanov is with Electronic and Electrical Engineering Department, University College London, London, WC1E 7JE, UK (e-mail: o.mitrofanov@ucl.ac.uk)

photo-currents produce a dominant contribution to the process of THz pulse generation. The effect is likely to be caused by unbalanced expansion of the electron-hole ensembles within the surface.

The process of photo-excited charge carrier redistribution in the surface plane is often ignored in describing the generation of THz pulses from semiconductor surfaces. Nevertheless we find that it can produce the majority of the radiated THz power: in the near-field region, the amplitude of the THz wave radiated from the edge is similar to that generated when the semiconductor surface is excited at an angle of incidence of 50°, the configuration considered optimum for THz pulse generation.

The photo-currents in the surface plane also explain the angular distribution of the generated THz waves in the far-field, which we characterize for InGaAs and GaAs surfaces excited at normal incidence. The experimental approach described here can provide insight to the role of metallic edges in the lateral photo-Dember effect in future studies.

II. Results

A. *Near-field mapping of generated THz pulses*

Mapping the emitted THz field in the near-field of the optical excitation area provides direct information about the spatial distribution of the photo-current responsible for THz pulse emission. To differentiate between the photo-current normal to the surface and parallel to the surface, we create two regions of optical excitation: a region where the density does not vary within the surface, and therefore the net photo-current is directed only normal to the surface, and a region where the density also changes with one spatial coordinate (x). In the latter case, both normal and lateral currents can be present.

This configuration is realized by exciting a semiconductor surface at normal incidence with a large diameter beam (FWHM=0.85 mm) through a relatively narrow slit of width w

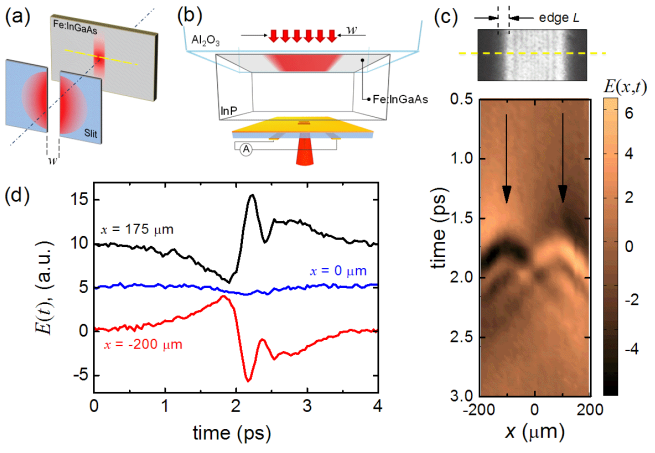

Fig. 1. Near-field mapping of the radiated THz field. Schematic diagrams of the experiment with excitation through a slit positioned within 1-5 mm from the Fe:InGaAs sample surface (a) and detection by a sub-wavelength aperture probe in the near-field zone (b). Space-time map of the radiated field THz field due to a 200 μm wide light strip (top panel). (d) Waveforms of the THz pulse field detected on the opposite sides of the strip (black and red) and in the strip center (blue).

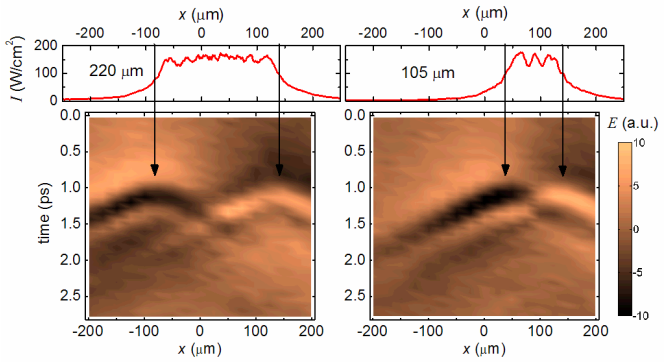

Fig. 2. Near-field distribution (space-time) of the THz field generated by the light strips of different width: 220 μm (left) and 105 μm (right). The optical intensity profiles $I(x)$ are shown in the top panels.

(adjustable in the range of 100-400 μm) [Fig. 1(a)]. This creates an optical excitation area in a form of a strip, with a uniform photo-carrier density within the strip area. For the excitation, we use short optical pulses (pulse duration: 100 fs, repetition rate: f_{rep} = 80 MHz, wavelength: λ = 800 nm). The excitation intensity is modulated by a mechanical chopper at 2.7 kHz similar to common THz time-domain spectroscopy systems.

A 1 μm thick epilayer of Fe:InGaAs is grown on an InP substrate [19]. The sample is attached to a transparent sapphire plate and the InP substrate is mechanically thinned to a thickness of 30 μm [Fig. 1(b)]. After the thinning, the substrate surface is polished to avoid scattering.

To map the emission of THz pulses in space and time, a THz near-field detector [20] is positioned ~40 μm away from the photo-excited surface [Fig. 1(b)]. This distance includes ~30 μm of the thinned InP substrate and ~10 μm of the air gap between the substrate and the probe. The THz probe has a metallic screen with a 10 μm × 10 μm aperture, through which the field of the generated THz pulse is sampled using a photoconductive THz antenna detector [20]. The THz detector is based on low-temperature grown GaAs with sub-picosecond carrier lifetimes [20].

Space-time maps of the generated THz pulses are recorded by scanning the light strip with respect to the THz detector [along the yellow dashed line in Fig. 1(a,c)], and by sampling the THz pulse in time. Photo-excited regions responsible for the THz pulse generation can therefore be identified using both the amplitude of the generated field, and the time of THz pulse arrival at the aperture.

To understand the effect of the photo-current direction on the detected near-field maps, it is useful to consider ideal dipole moments positioned in front of the probe aperture. Radiation from a dipole oriented within the surface plane is expected to couple into the probe most efficiently if it is aligned with the aperture center. Radiation from a dipole oriented perpendicular to the surface on the other hand couples into the probe only if the dipole is positioned to the left or to the right of the aperture center [21]. Therefore we expect different near-field signatures for the two orthogonal current directions.

A space-time map of the generated THz pulse for a 200 μm wide strip shows that the radiation originates from two well-defined locations corresponding to the strip edges [Fig. 1(c)]. These two sources produce similar THz pulses with opposite polarity [Fig. 1(d)]. In the center of the strip, the pulse amplitude reduces to zero as a result of destructive interference. The generated THz pulse amplitude increases linearly with the optical power and then starts saturating after the level of I=100 W/cm^2. This behavior confirms that the origin of the observed emission is a transient photo-current.

Remarkably, the amplitude of the generated THz field is independent of the light strip width. When one edge is moved while the other is kept at the same position, the generated THz field replicates the source movement [Fig. 2]. In the process of varying the strip width w from 105 to 340 μm, we do not observe any change in the detected THz pulse amplitude despite a substantial change in the optical excitation area, and the corresponding total number of photo-excited electron-hole pairs. Neither do we observe any significant variation of the emitted field amplitude with the edge sharpness, defined here by the characteristic length L, within which the excitation intensity drops to zero. When the edge sharpness L is varied from 30 μm [Fig. 1(c)] to 100 μm, the detected THz pulse peak amplitude near the edge remains practically unchanged. This suggests that the illumination intensity (per unit area), rather than the overall excitation power, determines the amplitude of emitted THz pulses.

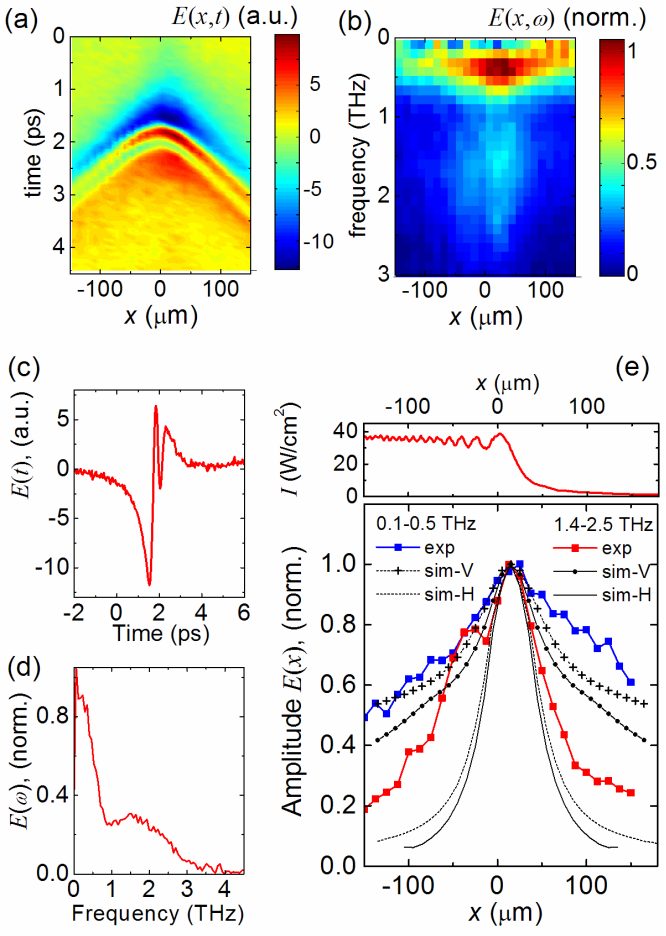

Fig. 3. THz field detected near the edge of photo-excited region: (a) space-time map and (b) frequency-domain representation of the field in (a). The pulse waveform (c) and spectrum (d) at the location of field maximum (x≈0). (e) Normalized THz pulse amplitude in the vicinity of the optical excitation edge for two spectral bands: 0.1-0.5 THz and 1.4-2.5 THz. Excitation intensity profile $I(x)$ near the edge is shown in the top panel.

The lack of amplitude dependence on the strip width indicates that the emission process can be studied in a simpler configuration – a single edge of an optically excited region. In this case, the interference between the THz pulses emitted from the opposite strip edges is eliminated. In order to simplify the analysis further, we also reduce the air gap between the sample and the probe to zero. The sample is in contact with the detector surface in the following experiments. All near-field distributions detected without the 10 μm air-gap are displayed in this article using a different color map [Fig. 3] to differentiate them from the measurements with the air gap [Figs. 1 and 2].

A time-domain map of THz emission due to a single edge and the corresponding frequency-domain map are shown in Figs. 3(a) and 3(b). The maps are almost symmetric despite the fact that the left-hand side of the sample is photo-excited and the right-hand side remains dark. There are two indications that the THz pulse is produced mainly in the region where the photo-excited carrier density changes along the surface. First of all, the field amplitude peaks in the region of the edge. Secondly, the delay in detection of the THz pulse is shortest near the edge; for any position of the edge with respect to the detector aperture, the delay is directly related to the travel time from the edge to the aperture (inside the InP substrate).

The THz pulse waveform [Fig. 3(c)] measured in the region of the maximum amplitude, similar to the waveforms in Fig. 1(d), exhibits slow and fast oscillations. They correspond to broad but well-defined spectral peaks at 0.25 THz and 1.5 THz [Figs. 3(b) and 3(d)]. The presence of two spectral peaks is not an artefact of the detector. It will be shown later that the low-frequency peak and the slow oscillation in the waveform disappear when the same detector is placed in the far-field.

These two components show noticeably different rates of decay with distance from the edge. The low-frequency field amplitude (integrated over 0.1-0.5 THz) decays by a factor of 2 at a distance of 125-150 μm from the edge, whereas the high-frequency field amplitude (1.4-2.5 THz) decays by a factor of 5 within the same distance [Fig. 3 (e)].

The two decay rates for the low- and high-frequency components however may represent different orientations of the photo-current vector. The radiation pattern for a dipole in the surface plane (oriented along the x axis) produces the maximum of emission in the z direction and decays to zero for emission in the x directions. A dipole normal to the surface plane on the other hand produces radiation along the surface and propagates further along the x axis. We therefore expect that the detected wave due to the photo-current in the surface plane decays faster with the distance from the edge (x) compared to the wave due to the normal current. This conclusion is confirmed by our numerical simulations presented in the next section.

B. *Numerical modeling of the radiated THz field*

The amplitude decay rate provides a quantitative measure for correlating the experimental near-field distribution with numerical simulations. We perform full wave numerical simulations of the sample and the near-field detector (with the aperture) for two idealized photo-current distributions: the photo-current normal to the surface with the spatial profile replicating the optical excitation intensity profile, and the photo-current in the surface plane distributed only in the region of the edge and directed perpendicular to the edge.

A schematic diagram of both models is shown in Fig. 4. The left-hand side of the diagram represents the current parallel to the surface, whereas the right-hand side represents the current normal to the surface. In the normal current case, the current amplitude is constant within the illuminated area and it decreases smoothly to zero, similar to the experimentally measured intensity profile [Fig. 3(e)]. For the in-plane photo-current, we assume that the current amplitude varies along the *x*-axis following a Gaussian function with the FWHM of 40 μm. The transient current is defined as a pulse of Gaussian profile with a FWHM of 360 fs. The transient solver (time domain finite-integration-technique) within the commercial solver (CST Microwave Studio) is then used to simulate the radiated field as well as the field detected by the near-field probe.

To account for the coupling of the radiated THz field through the sub-wavelength aperture of the near-field probe, the simulation includes the aperture in a gold metallic screen and the antenna of a photoconductive switch. The position of the probe is swept across the edge of the excitation area in steps of 10 μm. For each position, the simulated voltage across the gap of the antenna is recorded in time, providing a space-time map of the radiated field, as in the experiment. The simulation of the probe geometry ensures that the numerical results can be compared directly to the experiment despite the fact that these maps display a signal, which combines two electric field components, E_x and E_z [21,22].

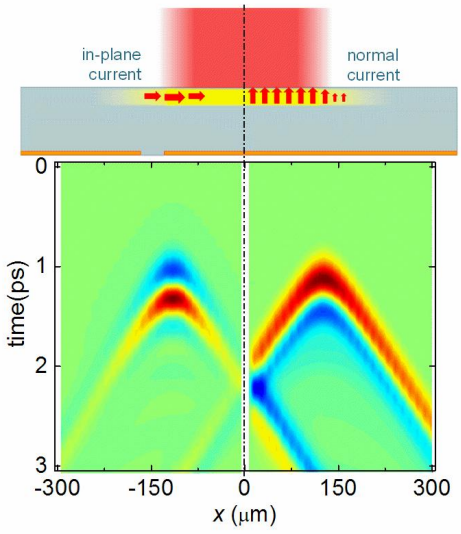

Fig. 4. Simulated THz field due to the in-plane photo-current (left) and the photo-current normal to the surface (right). The space-time maps (bottom) show the electric field of the THz pulse coupled through the near-field probe aperture. The aperture plane is separated from the photo-excited surface by the thinned InP substrate (30 μm). The schematic diagram (top) illustrates the distributions of transient photo-currents (red arrows).

The simulated space-time maps for the two photo-current distributions are shown in Fig. 4. These maps exhibit a similar pattern, representing a wave radiated from the edge. However for the current distribution in the direction normal to the surface, there is a substantially slower amplitude decay as the radiated wave propagates away from the edge. The amplitude decay can therefore be used to identify the photo-current responsible for generation of THz pulses.

The simulated amplitude of the radiated field for the two idealized current distributions are compared with the experiment for the low- and high- frequency bands in Fig. 3(e). The low-frequency band amplitude (0.1-0.5 THz) decreases in the experiment with a similar rate as the simulated field amplitude due to the current normal to the surface (sim-V). The high-frequency band (1.4-2.5 THz), on the other hand, decreases more rapidly, similar to the simulated field for the in-plane photo-current (sim-H). This suggests that the two frequency bands correspond to different photo-current orientations. We note that the photo-current distribution in the experiment is likely to include components with both orientations.

The idealized current models describe our experimental observations remarkably well. The comparison suggests that the high-frequency band observed in the experiment corresponds to the in-plane photo-currents that are often neglected in describing the THz pulse generation process. We will show in the following sections that the high-frequency

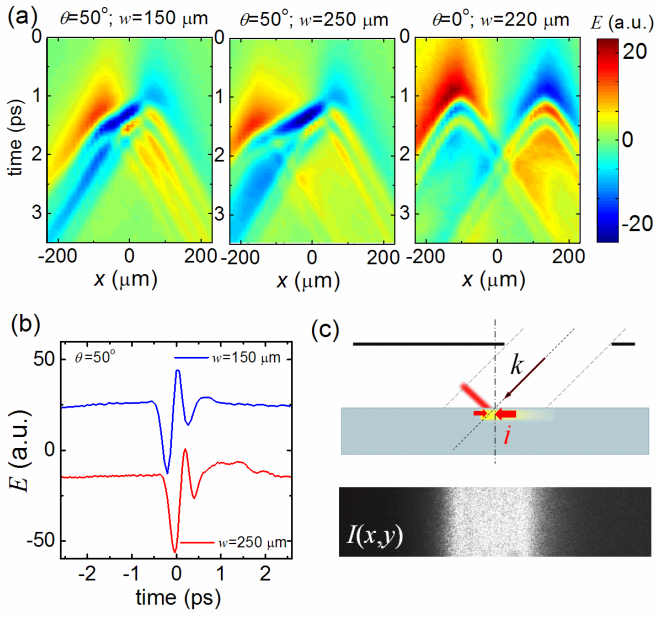

Fig. 5. THz field generated by the light strip incident on the surface at 50°. (a) Near-field space-time maps the for two strip widths: 150 μm (left) and 250 μm (center), compared to the normal incidence excitation (θ=0°). (b) Waveforms of the THz pulse detected in the region of the strip center (*blue*: *w*=150 μm; *red*: *w*=250 μm). (c) Schematic diagram of the surface excited at an angle showing the in-plane photo-current by red arrows. The corresponding time-averaged excitation intensity distribution *I*(*x*,*y*) is shown

band is the main contribution in the radiated THz field in the far-field.

C. Optimum generation of THz pulses

The optimum angle of incidence for generation of THz pulses is known to be to be 45°-75° [1-3]. In this section we consider the near-field distribution of the THz wave generated in the optimum configuration.

Near-field maps of the radiated field for an angle of incidence of 50° are compared for two strip widths (150 μm and 250 μm) to the map for the normal incidence excitation in Figs. 5(a). The excitation intensity (I=35 W/cm^2) and the color scale for the detected THz field are kept constant for comparison.

For the optimum incidence angle maps, the destructive interference (observed within the light strip for the normal incidence) changes to constructive interference. This is due to the optical excitation moving gradually from the right hand side to the left hand side of the light strip. The sources of the THz field nevertheless remain the same as in the normal incidence case.

Surprisingly, the near-field maps for the optimum configuration do not show a higher THz field amplitude compared to the normal incidence configuration. The difference between the excitations at normal incidence and at the optimum angle is found only in the spatial distribution of the radiated field.

The constructive interference within the strip builds up the total power of the radiated THz wave. Figure 5(a) illustrates this process. A blue streak, which corresponds to the peak of the THz pulse, is formed in the center of the illuminated area. The streak gets wider proportionally to the strip width, whereas its amplitude remains the same. Figure 5(b) show practically identical waveforms of THz pulses measured near the strip center for the different strip widths. While the local field amplitude remains constant, the total radiated power scales linearly with the strip width when the sample is illuminated at the optimum incidence angle.

The near-field maps allow us to identify the part of the optical pulse that makes the main contribution to the emission process. The 100 fs excitation pulse, which spans ~30 μm in the direction of propagation, effectively sweeps a ~45 μm wide strip of light across the sample surface (within the range defined by the slit width) [Fig. 5(c)]. Similarly to the normal incidence case, the edges of the 45 μm strip produce two THz sources of opposite polarity, corresponding to the leading and trailing parts of the excitation pulse.

The blue streak in the experimental maps indicates that the radiated THz field originates from the trailing part of the optical pulse, or the right-hand side edge of the light strip. The photo-current produced by the leading front of the optical pulse is likely to be suppressed as the optical excitation sweeps across the surface faster than the charge carriers, eliminating the carrier density gradient on one side. The suppression of the photo-current due to the leading edge occurs everywhere within the range of the slit. The trailing edge on the other hand now produces THz emission as it sweeps across the surface.

The waveforms in Fig. 5(b) also show that the low-frequency oscillation of the field at the start of the THz pulse [Fig. 3(c)] is noticeably reduced in the central area. We attribute this effect to interference as well. Similarly to the case of normal incidence [Fig. 2], the destructive interference effect for the effectively narrow strip of 45 μm is more severe at lower frequencies.

The near-field THz emission maps for the optical excitation at normal incidence and at the optimum angle show that THz fields of similar amplitudes are generated in the two cases. Therefore we conclude that the same photo-currents are responsible for THz generation in both configurations. However for the excitation at the optimum angle, the high-frequency component of the THz field forms a coherent wave-front moving along the direction of the optical axis. Using our analysis of the near-field distribution for a single edge, we conclude that the high-frequency component originates from the photo-currents in the surface plane, rather than the photo-current driven in the normal direction.

III. Discussion

Based on the presented experimental and numerical results, the role of in-plane photo-currents in the process of THz pulse generation should not be neglected, particularly when the optical excitation area is comparable or larger than ½ of the THz wavelength. Variation of the photo-carrier density along the surface is identified as an essential requirement for efficient generation of the THz field in our samples (Fe:InGaAs). This variation is created due to the shape of the optical excitation beam at normal incidence or due to the 'sweeping' of short optical pulses along the surface when it is excited at an angle.

A. Photo-excited charge carrier dynamics

The lateral photo-Dember effect model can provide an explanation for the observed effects. We note however that a

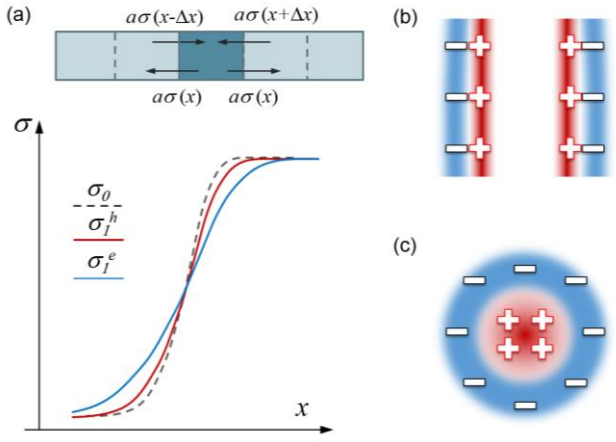

Fig. 6. Photo-excited charge density evolution. (a) Charge carrier flow in and out of a unit area $\Delta\sigma = a(\sigma(x-\Delta x)+\sigma(x+\Delta x)-2\sigma(x))$, where a represents a fraction of the carriers that cross the area boundary (top); density distribution $\sigma(x)$ for electrons and holes at the moment of excitation (σ_0) and after the excitation (σ_l^e, σ_l^h). Charge separation within the surface for the optical excitations through a slit (b) and for the excitation by a focused laser beam (c).

relatively small gradient of the photo-carrier density within the surface plane is sufficient to generate THz pulses. It suggests that further refinement of the lateral drift-diffusion model is required. A rigorous model for the emission process is beyond the scope of this study. We nevertheless suggest considering the photo-current contribution due to the initial momentum of the photo-excited charge carriers.

The charge carriers are created with a large initial momentum for the optical excitation with the photon energy substantially above the bandgap (E_G≈0.75 eV for InGaAs). In a region of uniform optical excitation, the overall photo-current due to this initial momentum averages to zero as any direction is equally probable. However, there will be a flow of charge carriers from regions of higher density to regions of smaller density if the optical excitation intensity varies along the surface [Fig. 6(a)]. A large difference in effective masses for electrons and holes creates imbalance in this charge flow. This effect results in initial expansion of the electron-hole ensembles even before the carriers thermalize, i.e. before their dynamics can be described by the diffusion equation.

The process of charge cloud expansion is schematically illustrated in Fig. 6(b) for the case of a strip of light projected on the surface at normal incidence, as we discussed earlier, and in Fig. 6(c) for a Gaussian optical beam. A higher electron density $\sigma^e > \sigma^h$ is formed temporally outside the excitation area and a higher hole density $\sigma^h > \sigma^e$ is formed inside the area [Fig. 6(b,c)]. The transient charge imbalance near the edge (transient polarization) then causes the radiation of a THz pulse.

Monte-Carlo simulations of the carrier dynamics, considered more recently in Ref. 18, can describe the initial expansion process as well as the drift-diffusion dynamics fully.

B. *Angular emission pattern in the far-field zone*

Validity of the in-plane transient polarization (or transient current) model can be tested in predicting the angular distribution of the radiated THz wave. If a semiconductor surface is excited at normal incidence, no THz pulses are emitted exactly in the direction of the optical axis in the far-field. The model explains this effect as a result of the symmetric distribution of the photo-current in the surface plane. The radiated field nevertheless is expected in directions off the optical axis with a maximum in the range of 20°–50° depending on the spatial profile of the optical excitation. The angular emission pattern can be measured in our experimental system and used to verify the model [23].

IV. FAR-FIELD TERAHERTZ EMISSION

A schematic diagram of the experimental system for mapping the amplitude of emitted THz pulses as a function of the emission angle is shown in Fig. 7(a). A Fe:InGaAs sample is excited by a weakly focused beam (FWHM: 250 μm, average power of 350 mW). The beam is positioned 2 mm away from the sample cleaved edge. A THz photoconductive detector with a sub-wavelength input aperture (D2), is now positioned in the far-field zone, at a distance of 5 mm [Fig. 7(a)]. A similar second detector, D1 is positioned on the side of the sample, 1.2 mm from the sample edge. The aperture plane for detector D1 (D2) is oriented normal to the *x*-axis (*z*-axis). The detectors are in the far-field region of the excitation spot: the distance between the source and the detector is at least 3.2 mm, which is much larger than the THz wavelength (100-500 μm in these experiments) and the Rayleigh range of the THz source ($z_R \approx 500$ μm).

The configuration in Fig. 7(a) allows us to map the angular distribution without changing the detector positions. In the half-space above the sample surface, the distribution can be mapped between angles θ_1 = 20°–90° with detector D1 by translating the focusing lens and the sample together along the optical axis (*z*). To probe the emission guided in the substrate by total internal reflection, the sample's cleaved edge is positioned facing the detector (θ_1 = 90°-100°). Below the sample surface, the angular distribution is obtained for angles θ_2 = 180°– θ_1 = 0-48° with detector D2 by translating the excitation beam and the sample along the *x*-axis [Fig. 7(a)].

We note that the THz wave is incident on detectors D1 and D2 at angles θ_i = 90-θ_1 and θ_i = θ_2 respectively. We evaluated the sensitivity of our sub-wavelength aperture detector numerically (CST) and found that the sensitivity to the incident THz radiation polarized in the *xz*-plane is independent of the angle of incidence for the angular ranges considered here (θ_i < 70). Results of this sensitivity study will be published elsewhere. The detector orientation therefore is not adjusted during the measurements. Divergence of the radiated wave in the far-field is taken into account by scaling the amplitude of the detected THz field by the inverse distance between the point of excitation and the detector (1/*r*).

The THz detector for the far-field measurement comprises a photo-conductive antenna and a 50 μm x 50 μm input aperture

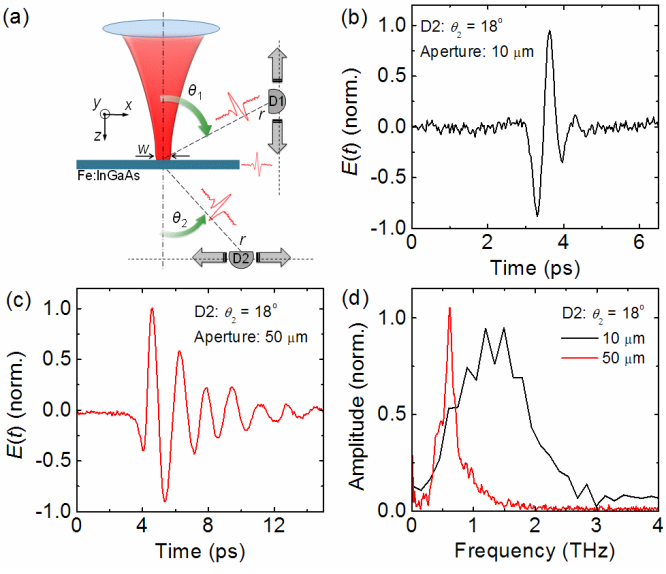

Fig. 7. (a) Schematic diagram of the experimental system for measurements of the angular emission pattern; D1 and D2 represent THz detectors. (b, c) Normalized waveforms of the THz pulse measured at θ_2=18° by detectors with the 10 μm and 50 μm input apertures and the corresponding spectra (d).

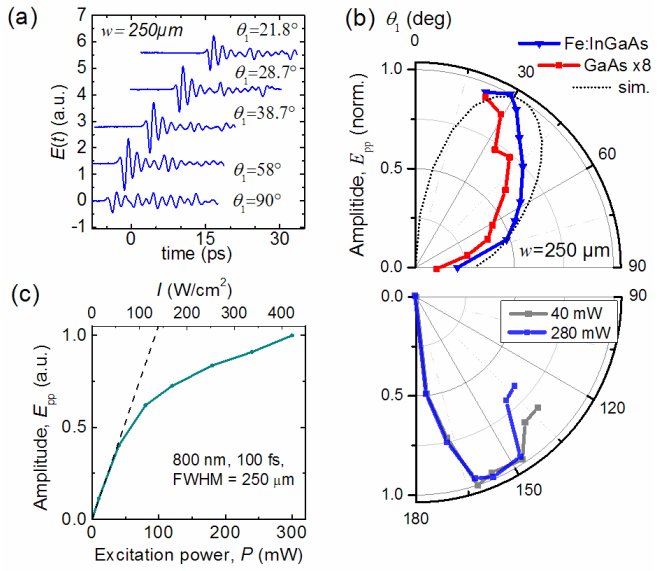

Fig. 8. (a) THz pulse detected by detector D1 for θ_1 ranging from 20° to 90° after excitation of Fe:InGaAs by the 250 μm diameter laser beam. (b) Angular distribution of the radiated field (peak-to-peak amplitude E_{pp}). The top panel shows normalized emission patterns for Fe:InGaAs and GaAs and the excitation power of P=350 mW, and the bottom panel shows normalized emission patterns for Fe:InGaAs and P= 40 mW and 280 mW. The black line shows the simulated emission pattern for the in-plane current distribution.

[20]. The larger aperture provides a substantially larger detected signal and thus a higher dynamic range compared with the 10 μm aperture [24]. The aperture is nevertheless small enough to resolve the direction of the radiated THz wave with accuracy of ~1°. A disadvantage of the 50 μm aperture probe is however its resonant response near the aperture cut-off frequency of ~0.6-0.7 THz [24], which alters the pulse shape. We therefore use the 10 μm aperture detector first to analyze the spectrum of the radiated THz pulses.

A typical waveform in the transmission configuration (detector position D2) is shown in Fig. 7(b) for the detector located at θ_2 = 18°. The far-field pulse is similar to the near-field detected pulse, however the low-frequency oscillation that we associate with the emission due to the current normal to the surface is absent. We note that the same detector was used for the measurements presented in Figs. 1-3.

The waveform measured when the 10 μm aperture probe is replaced by the 50 μm aperture probe is significantly higher in amplitude. The waveform however displays the typical response of the 50 μm aperture with a spectral peak near the aperture cut-off frequency [Figs. 7(c) and 7(d)] [21].

Selected waveforms of the THz pulses emitted above and along the surface (θ_1 = 90°) are shown in Fig. 8(a). The pulse amplitude shows strong dependence on the emission angle. We find that the amplitude exhibits a maximum for θ_1 = 20–30° (above the surface) and for θ_1 = 150-165° (below the surface, θ_2 = 15-30°) [Fig. 8(b)]. There is practically no emission in the direction normal to the surface. Along the surface, θ_1 = 90°, the amplitude is small and the waveform contains two contributions: the earlier pulse corresponds to the wave travelling through air along the surface and the later pulses (t > 5 ps) correspond to the wave travelling inside the sample substrate. The angular distribution remains unchanged for the excitation power below the saturation threshold P=40 mW [Fig. 8(b), bottom panel] and slightly above it P=280 mW.

The amplitude of the generated THz pulse decreases substantially when the diameter of the optical excitation is reduced from ~250 μm to ~60 μm. When the excitation diameter is increased above ~250 μm, the amplitude decreases slowly as well. Such a behavior supports the model of in-plane dipoles on the opposite sides of the excitation spot. The two dipoles interfere destructively when they are separated by less than ½ of the wavelength in free space. For the excitation diameter of ~ ½ of the wavelength, the interference is constructive. For larger diameters, it becomes destructive again.

Full wave time domain simulations of the emission pattern are performed also in CST. We model the transient in-plane photo-current as 2 μm long current sources distributed within a 250 μm diameter ring according to the model presented in Fig. 6(c). The current sources are placed 1 μm under the InP surface and their vectors are directed toward the ring center. The current transient is defined as a short pulse to cover the frequency range from 0.2 THz to 1 THz and to match the frequency content of the wave detected experimentally.

The amplitude of the radiated THz pulse is recorded in the simulations for angles θ_1 = 0-90° at a distance of 5 mm from the ring center. The simulated angular emission pattern is compared to the experimentally measured amplitude in Fig. 8(b). The close match validates the model of in-plane photo-current distribution. Simulations of the photo-current normal to the surface on the other hand predict an emission pattern with its maximum at a larger angle. We also note that a unit photo-current normal to the surface produces a substantially weaker THz emission according to the numerical simulations.

V. Conclusion

The near-field and far-field properties of the THz pulse field radiated from photo-excited Fe:InGaAs surfaces suggest that the photo-excited charge carrier dynamics in the plane of the surface play a key role in the process of THz pulse generation, particularly when the size of the optical excitation is comparable to ½ of the wavelength. The experimental results show direct correlation of the emitted wave with regions of photo-excited charge carrier density gradient in the surface plane. The results suggest that the commonly accepted model that links the process of THz pulse generation to the transient photo-current normal to the surface may need to be refined. We suggest that the unbalanced expansion of photo-excited electron and hole ensembles within the surface may be leading to the generation of THz pulses in Fe:InGaAs. The experimental approach described here can be applied further to investigate the role of metallic edges in the lateral photo-Dember effect.

The observed effect is not unique to Fe:InGaAs. The amplitude of emitted THz pulses from Fe:InGaAs is however

twice as high compared to InGaAs without Fe doping. A semi-insulating GaAs sample produces a similar emission pattern, however the amplitude of the emitted field is reduced further (by ~8 times) [Fig. 8(b)]. The role of material properties in the generation process is beyond the scope of this study, we note however that a number of previous studies have shown that the smaller effective mass in InGaAs compared to GaAs, and the shorter carrier lifetime due to the Fe doping improve the efficiency of THz pulse generation [19,265]. The impact of material parameters on the emission process can help verifying the transient current model in future studies.

One unexpected finding of this study is that the optical excitation of InGaAs at normal incidence produces a THz wave with a similar amplitude as the excitation at the optimum angle. At normal incidence however, the THz emission is directed mainly at 20-30° from the optical axis and it depends on the size of the photo-excited region.

The correlation of the emitted THz field with the regions of photo-excited charge carrier density variation suggests that THz emission can be tailored and optimized by shaping the spatial and temporal profiles of the optical excitation. Alternatively optical excitation with Gaussian beams at normal incidence can be used to match selected modes in THz waveguides, e.g. the fundamental mode of a coaxial waveguide.

REFERENCES

[1] X.-C. Zhang, B.B. Hu, J.T. Darrow, and D.H. Auston, "Generation of femtosecond electromagnetic pulses from semiconductor surfaces," *Appl. Phys. Lett.* **56**(11), 1011-1013 (1990).

[2] X.-C. Zhang and D.H. Auston, "Optoelectronic measurement of semiconductor surfaces and interfaces with femtosecond optics," *J. App. Phys.* **71**(1), 326-338 (1992).

[3] H. G. Roskos, M. C. Nuss, J. Shah, K.l Leo, D. A. B. Miller, A. M. Fox, S. Schmitt-Rink, and K. Köhler, "Coherent submillimeter-wave emission from charge oscillations in a double-well potential," *Phys. Rev. Lett.* **68**, 2216 (1992).

[4] P. C. M. Planken, M. C. Nuss, I. Brener, K. W. Goossen, M. S. C. Luo, S. L. Chuang, and L. Pfeiffer, "Terahertz emission in single quantum wells after coherent optical excitation of light hole and heavy hole excitons." Phys. Rev. Lett. **69**(26), 3800 (1992).

[5] J. N. Heyman, P. Neocleous, D. Hebert, P. A. Crowell, T. Müller, and K. Unterrainer, "Terahertz emission from GaAs and InAs in a magnetic field," *Phys. Rev. B* **64**(8), 085202 (2001).

[6] M. B. Johnston, D. M. Whittaker, A. Corchia, A. G. Davies, and E. H. Linfield, "Simulation of terahertz generation at semiconductor surfaces," *Phys. Rev. B* **65**(16), 165301 (2002).

[7] J. N. Heyman, N. Coates, A. Reinhardt, and G. Strasser, "Diffusion and drift in terahertz emission at GaAs surfaces," *Appl. Phys. Lett.* **83**(26), 5476-5478 (2003).

[8] K. Liu, J. Xu, T. Yuan, and X.-C. Zhang, "Terahertz radiation from InAs induced by carrier diffusion and drift," *Phys Rev. B* **73**(15), 155330 (2006).

[9] A. Reklaitis, "Crossover between surface field and photo-Dember effect induced terahertz emission," J. Appl. Phys. **109**(8), 083108 (2011).

[10] A. Reklaitis, "Terahertz emission from InAs induced by photo-Dember effect: Hydrodynamic analysis and Monte Carlo simulations," *J. Appl. Phys.* **108**(5), 053102 (2010).

[11] I. Wilke, Y. J. Ding, and T. V. Shubina, "Optically- and electrically-stimulated terahertz radiation emission from Indium Nitride," *J Infrared Milli Terahz Waves* **33**, 559-592 (2012).

[12] H. Dember, *Physik. Z.* **32**, 554, (1931).

[13] G. Klatt, F. Hilser, W. Qiao, M. Beck, R. Gebs, A. Bartels, K. Huska, U. Lemmer, G. Bastian, M.B. Johnston, M. Fischer, J. Faist, and T. Dekorsy, "Terahertz emission from lateral photo-Dember currents," *Opt. Express* **18**(5), 4939-4947 (2010).

[14] G. Klatt, B. Surrer, D. Stephan, O. Schubert, M. Fischer, J. Faist, A. Leitenstorfer, R. Huber, and T. Dekorsy, "Photo-Dember terahertz emitter excited with an Er:fiber laser," *Appl. Phys. Lett.* **98**, 021114 (2011).

[15] W. Qiao, D. Stephan, M. Hasselbeck, Q. Liang, and T. Dekorsy, "Low-temperature THz time domain waveguide spectrometer with butt-coupled emitter and detector crystal," *Opt. Express* **20**(18), 19769-19777 (2012).

[16] M.E. Barnes, S.A. Berry, P. Gow, D. McBryde, G.J. Daniell, H.E. Beere, D.A. Ritchie, and V. Apostolopoulos, "Investigations of the role of the lateral photo-Dember effect in the generation of terahertz radiation using a metallic mask on a semiconductor," *Opt. Express* **21**(14), 16263-16272 (2013).

[17] M.E Barnes, D. McBryde, G.J. Daniell, G. Whitworth, A.L. Chung, A.H. Quarterman, K.G. Wilcox, A. Brewer, H.E. Beere, D.A. Ritchie, and V. Apostolopoulos, "Terahertz emission by diffusion of carriers and metal-mask dipole inhibitation of radiation," *Opt. Express* **20**(8), 8898-8906 (2012).

[18] M. E. Barnes, G. J. Daniell, P. Gow, and V. Apostolopoulos "Simulation of Terahertz Generation from Lateral Diffusion Currents in Semiconductor Devices," *J. IRMMW-THz* **35** (12), 1030-1044 (2014).

[19] O. Hatem, J. Cunningham, E.H. Linfield, C.D. Wood, A.G. Davies, P.J. Cannard, M.J. Robertson, and D.G. Moodie, "Terahertz-frequency photoconductive detectors fabricated from metal-organic chemical vapor deposition-grown Fe-doped InGaAs," *Appl. Phys. Lett.* **98**(12), 121107 (2011).

[20] O. Mitrofanov, M. Lee, J.W.P. Hsu, I. Brener, R. Harel, J.F. Federici, J.D. Wynn, L.N. Pfeiffer, and K.W. West, "Collection-mode near-field imaging with 0.5-THz pulses," *IEEE J. Sel. Top. Quant. Electr.*, **7**(4), 600-607 (2001).

[21] R. Mueckstein and O. Mitrofanov, "Imaging of terahertz surface plasmon waves excited on a gold surface by a focused beam," *Opt. Express* **19**(4), 3212-3217 (2011).

[22] M. Natrella, O. Mitrofanov, R. Mueckstein, C. Graham, C. C. Renaud, and A. J. Seeds, "Modelling of surface waves on a THz antenna detected by a near-field probe," *Opt. Express* **20**(14), 16023-16031 (2012).

[23] R. Mueckstein, M. Natrella, O. Hatem, J. R. Freeman, C. S. Graham, C. C. Renaud, A. J. Seeds, E. H. Linfield, A. G. Davies, P. J. Cannard, M. J. Robertson, D. G. Moodie, and O. Mitrofanov, "Mapping the distribution of photo-currents responsible for generation of terahertz pulses at semiconductor surfaces," in *Proc. IRMMW-THz, 39th International Conference*, pp. 1-2. IEEE, 2014.

[24] O. Mitrofanov, M. Lee, J.W.P. Hsu, L.N. Pfeiffer, K.W. West, J.D. Wynn, and J.F. Federici, "Terahertz pulse propagation through small apertures," *Appl. Phys. Lett.* 79, 907 (2001).

[25] J. Mangeney and P. Crozat, "Ion-irradiated $In_{0.53}Ga_{0.47}As$ photoconductive antennas for THz generation and detection at 1.55μm wavelength," *C.R. Physique* **9**, 142-152 (2007).